energies

MDPI

Article

Dynamic Mechanical and Microstructural Properties of Outburst-Prone Coal Based on Compressive SHPB Tests

Zhenhua Yang [1], Chaojun Fan [1,*], Tianwei Lan [1,2], Sheng Li [1], Guifeng Wang [2], Mingkun Luo [1,3] and Hongwei Zhang [1,*]

[1] College of Mining, Liaoning Technical University, Fuxin 123000, China; 471710043@lntu.edu.cn (Z.Y.); lantianwei@lntu.edu.cn (T.L.); lisheng@lntu.edu.cn (S.L.); qqluomingkun@126.com (M.L.)

[2] State Key Laboratory of Coal Resources and Safe Mining, School of Mines, China University of Mining and Technology, Xuzhou 221116, China; wgfskl@cumt.edu.cn

[3] Center of Technology, Shanxi Lu'an Mining (Group) Limited Liability Company, Changzhi 046299, China

* Correspondence: chaojunfan@139.com (C.F.); kyzhw@263.net (H.Z.)

Received: 5 October 2019; Accepted: 5 November 2019; Published: 6 November 2019

Abstract: Understanding the dynamic mechanical behaviors and microstructural properties of outburst-prone coal is significant for preventing coal and gas outbursts during underground mining. In this paper, the split Hopkinson pressure bar (SHPB) tests were completed to study the strength and micro-structures of outburst-prone coal subjected to compressive impact loading. Two suites of coals—outburst-prone and outburst-resistant—were selected as the experimental specimens. The characteristics of dynamic strength, failure processes, fragment distribution, and microstructure evolution were analyzed based on the obtained stress-strain curves, failed fragments, and scanning electron microscopy (SEM) and nuclear magnetic resonance (NMR) images. Results showed that the dynamic compressive strength inclined linearly with the applied strain rate approximately. The obtained dynamic stress-strain responses could be represented by a typical curve with stages of compression, linear elasticity, microcrack evolution, unstable crack propagation, and rapid rapture. When the loading rate was relatively low, fragments fell in tension. With an increase in loading rates, the fragments fell predominantly in shear. The equivalent particle size of coal fragments decreased with the applied strain rate. The Uniaxial compressive strength (UCS) of outburst-prone coal was smaller than that of resistant coal, resulting in its smaller equivalent particle size of coal fragments. Moreover, the impact loading accelerated the propagation of fractures within the specimen, which enhanced the connectivity within the porous coal. The outburst-prone coal with behaviors of low strength and sudden increase of permeability could easily initiate gas outbursts.

Keywords: outburst-prone coal; split Hopkinson pressure bar; dynamic strength; fragment distribution; microstructural characteristics

1. Introduction

Coal is an important source of fossil energy. During underground coal mining, coal and gas outburst usually occurs [1,2]. This dynamic disaster would suddenly eject a large amount of gases accompanying extensive coals [3], resulting in significant damage to equipment and may even cause fatalities [4]. Many exploratory investigations on this catastrophic phenomenon have been conducted to obtain a better understanding of the causative mechanisms and better preventive treatment for outbursts [5–11]. The characteristics of short occurrence duration, high intensity, and strong damage made it scarcely possible to obtain geo-stress and gas pressure immediately, as well as to gain mechanical properties of coals under various impact loadings [12–14]. At present, most researchers are convinced that outbursts will occur when the combination of abnormal crustal stress, high gas pressure, and outburst-prone coal stands a critical threshold [15,16]. The difference of these theories lies in the different reasons for forming this critical threshold, such as faults, folds, gas pockets, coal thickness, water content, gas adsorption capacity, etc. [17–24]. Generally speaking, coal and gas outburst is more likely occurred in the tectonically deformed thick coals usually with a structure of cataclastic band in the middle [25]. However, outbursts may also occur in the homogenous coal seam without geological disturbances if the gas pressure and geo-stress reach a critical threshold [26]. Even though they have a common ground, outburst-prone coal is the main material basis of gas outbursts [27]. The outburst-prone coal is usually featured by the static natures of low strength (pockets or continuous layers of weak, friable, and powdery medium) [28], the high initial velocity of gas emission [29], and strong gas sorption affinity [30]. The dynamic failure characteristics of outburst-prone coal under impact loadings are important to reveal the outburst mechanism [31,32].

The dynamic failure characteristics of coal and rock have gradually attracted more current attention [33–35]. The experimental testing methods are mainly applied to explore the dynamic properties of coal and rock, such as wave velocity, porosity, strength, scale effect, bedding effect, moisture effect, and energy dissipation [36–43]. Dynamic tests are completed by the split Hopkinson pressure bar (SHPB) apparatus [44–46]. This apparatus is well-known as an ideal and reliable device to test the dynamic properties of brittle mediums, including concretes [47], ceramics [48], rocks [49,50], and coals [51,52], under a wide range of impact loadings or strain rates. The main achievements are focused on the dynamic stress-strain curves and the relationship among the elastic modulus, compressive/tensile strength, and strain rate [53]. According to previous works, the dynamic SHPB tests on rock and common coal materials have been carried out extensively; however, only a few dynamic tests were on outburst-prone coal. In addition, most of these experiments only obtained the dynamic stress-strain curve, rather than the fragment characteristics and the microscopic characteristics of dynamic failure of outburst-prone coal, let alone the difference of dynamic failure characteristics between outburst-prone and resistant coals.

In the present work, two suites of experiments on coals—outburst-prone and outburst-resistant specimens—were conducted to investigate the strength and micro-structures of outburst-prone coal under the compressive impact loading. The dynamic mechanical properties of both outburst-prone and resistant coals were comparatively investigated and discussed. The fragment behavior and microstructure evolution of the crushed outburst-prone coal were studied using SEM and NMR technologies. These results gave important insights into the mechanism of gas outbursts.

2. Laboratory Specimen and Test Setup

2.1. Specimen Procurement and Preparation

Two coal types—outburst-prone and outburst-resistant—were collected from No. 4 coal seam in Xintian mine and No. 11 coal seam in Xinzhouyao mine, respectively, for testing. According to the International Society of Rock Mechanics (ISRM) suggested method, the specimens with slenderness ratio L/D = 1:1 (50 mm × 50 mm) were drilled from the collected fresh and large coal blocks for dynamic uniaxial compressive strength tests [54]. Both sides of coal specimens were cut and ground to satisfy the hypothesis of a one-dimensional elastic wave during the impact test. The prepared coal specimens are shown in Figure 1a,b.

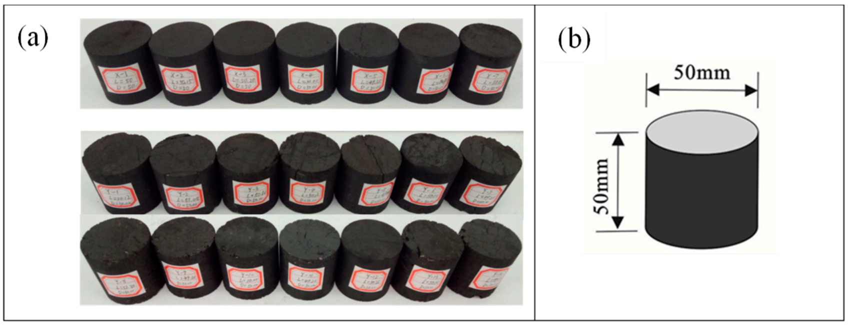

Figure 1. Preparation of experimental coal specimens: (**a**) photograph of prepared specimens, (**b**) geometry size of the specimen.

The Xintian (outburst-prone) coal is anthracite with a vitrinite reflectance (Ro) of ~2.13%, moisture content (Mad) of ~1.91%, ash content (Aad) of ~23.28%, volatile matter (Vad) of ~8.81%, and fixed carbon (FCad) of ~66.00%, as measured by proximate analysis. Meanwhile, the Xinzhouyao (outburst-resistant) coal is bituminous coals with a vitrinite reflectance (Ro) of ~0.85%, moisture content (Mad) of ~5.83%, ash content (Aad) of ~14.35%, volatile matter (Vad) of ~2.32%, and fixed carbon (FCad) of ~57.50%. The quasi-static mechanical properties of the coal specimens were measured by an MTS815 testing system. The results of these tests are shown in Table 1.

Table 1. Physical and quasi-static mechanical properties of coal specimens.

Specimen	Dry Density, ρ_d (g/cm^3)	Uniaxial Compressive Strength, σ_c (MPa)	Tensile Strength, σ_t (MPa)	Elastic Modulus, E_t (GPa)	Poisson Ratio, ν
Xintian coal (prone)	1.36	4.76	0.68	2.34	0.28
Xinzhouyao coal (resistant)	1.29	11.45	1.45	3.98	0.24

2.2. Apparatus and Basic Principles for SHPB Tests

The dynamic compressive strength tests on both, outburst-prone and outburst-resistant, coals were conducted using the SHPB system. The schematic diagram of the SHPB system is given in Figure 2. The setup includes launching unit, pressure bars, absorption unit, signal measuring, and processing unit. The launching unit includes high-pressure gas cylinder and gas gun; the pressure bar part includes a striker bar (made of Cr40 alloy steel, 37 mm in diameter and 300 mm in length), an incident bar (50 mm in diameter and 2400 mm in length, with a transition diameter of 37 mm from 600 mm to the striker bar contact end), and a transmitted bar (50 mm in diameter and 1400 mm in length); the absorption unit includes an absorbing bar and a deceleration device. The signal acquisition and processing system part include strain gauges and a data acquisition unit, with a sampling rate of ~10 million, and a data processing device, with the functions of filtering noise signals and analyzing results. The elastic modulus of pressure bars is 210 GPa. The transport speed of stress wave in the pressure bars is 5190 m/s. The length of the strain gauge is 6.35 mm, and the resistance is ~120 Ω.

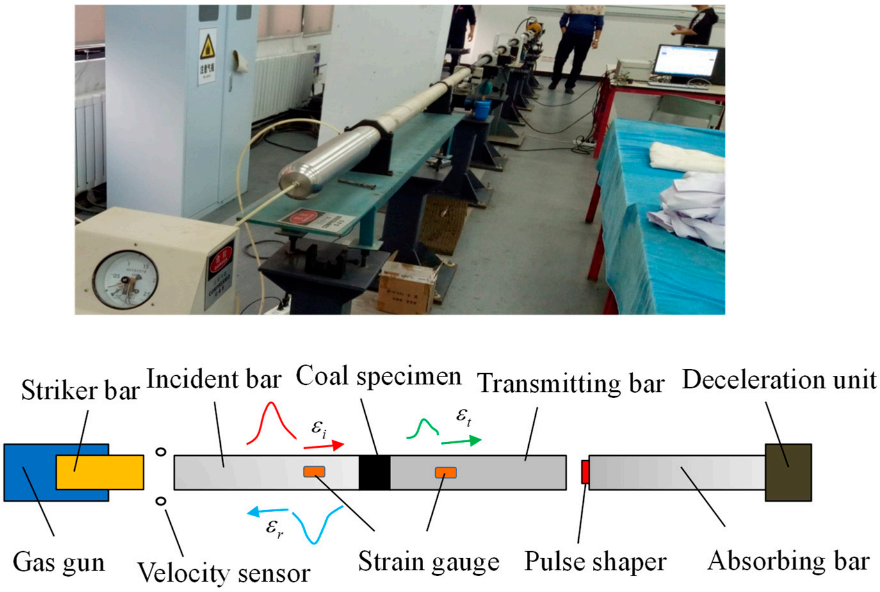

Figure 2. The apparatus and schematic diagram of a split Hopkinson pressure bar (SHPB) system.

To gain the dynamic properties of the coal specimen accurately, a square rubber sheet is adopted as the pulse shaper. It can transform the incident stress wave from a rectangle like a shape into an approximately semi-sinusoidal shape. The vaseline reagent is applied to both ends of coal specimens to avoid transverse strains.

During SHPB tests, the specimen is located between the incident and transmitted bars. The striker bar will be driven by a gas gun to collide with the incident bar, and thus stress waves will be generated (incident compressive pulse, ε_i). The stress wave then will transport within the incident bar and impact the coal specimen, causing a high-rate of deformation. When stress wave transports to the contact area of the coal specimen and incident bar, parts of the stress wave will transport back to the incident bar to be the reflected wave, ε_r. Meanwhile, other waves will go through the specimen and enter the transmitted bar to be the transmitted wave, ε_t. These wave signals will be measured and recorded by strain gauges and data acquisition devices, respectively.

Wave theory is adopted to express the stress-strain curve of the coal material [32]:

$$\begin{cases} \dot{\varepsilon}(t) = \frac{C_b}{L_s}(\varepsilon_i - \varepsilon_r - \varepsilon_t) \\ \varepsilon(t) = \frac{C_b}{L_s}\int_0^t (\varepsilon_i - \varepsilon_r - \varepsilon_t)dt \\ \sigma(t) = \frac{A_b}{2A_s}E_b(\varepsilon_i + \varepsilon_r + \varepsilon_t) \end{cases} \tag{1}$$

where E_b is elastic modulus of the pressure bar, GPa; C_b is the velocity of the stress wave in the pressure bar, m/s; A_b is the cross-sectional area of the pressure bar, m^2; A_s is the original cross-sectional area of the coal specimen, m^2; and L_s is the length of coal specimen, m.

The impact stress at two sides of coal specimen can be calculated as [49]:

$$\begin{cases} P_1(t) = A_b E_b(\varepsilon_i + \varepsilon_r) \\ P_2(t) = A_b E_b \varepsilon_t \end{cases} \tag{2}$$

Based on the stress-homogeneity hypothesis, the force equilibrium at two sides of the coal specimen can be achieved by satisfying $P_1(t) = P_2(t)$. The above equation can be rewritten as [33]:

$$\varepsilon_i + \varepsilon_r = \varepsilon_t \tag{3}$$

By submitting Equation (3) into Equation (1), the strain rate, dynamic strain, and dynamic stress are recovered as:

$$\begin{cases} \dot{\varepsilon}(t) = -\frac{2C_b}{L_s}\varepsilon_r \\ \varepsilon(t) = -\frac{2C_b}{L_s}\int_0^t \varepsilon_r dt \\ \sigma(t) = \frac{A_b}{A_s}E_b\varepsilon_t \end{cases} \quad (4)$$

Therefore, the stress-strain curve of coal samples under dynamic loadings can be recovered by calculating the measured signals of the reflected and transmitted pulses. The force equilibrium is achieved by the small slenderness ratio of prepared specimens, as well as perfect contact among pressure bars and coal specimens. The slenderness ratio L/D = 1:1 is selected for uniaxial compressive strength SHPB tests.

2.3. Methodology and Apparatus of SEM and NMR Tests

The FEI-Q45 type energy spectrum scanning electron microscopy (SEM) and MacroMR12-150H-I type low field nuclear magnetic resonance system (NMR) were applied to test microstructural characteristics of the crushed coal specimens after SHPB tests. The apparatus of SEM and NMR tests are shown in Figure 3.

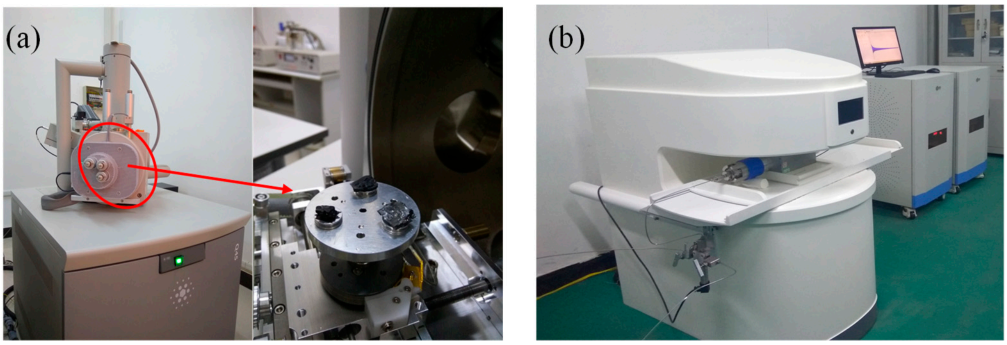

Figure 3. Apparatus of (**a**) SEM and (**b**) NMR tests.

The equipment has three working modes: high vacuum, low vacuum, and environment vacuum. When the accelerating voltage is 30 kV, the resolution of the Se image is less than 3.0 nm, and that of the Backscattered Scanning Electron (BSE) image is less than 4.0 nm. With the decrease of accelerating voltage, the resolution decreases. The accelerating voltage is 200–300 kV, and the magnification is 60–1000 thousand times. The process of SEM tests on SHPB cracked coals mainly includes the following three steps: firstly, paste the coal sample to be observed on the acetone soaked tray; secondly, put the tray with coal sample on the equipment loading platform, and start vacuuming; thirdly, when the vacuum reaches the standard value, set the acceleration voltage, magnification, and other parameters, observe, and photograph.

NMR imaging measures changes in the spin magnetic moment of the ^{1}H nucleus under the action of an external magnetic field. When the external magnetic field disappears, the spin magnetic moment gradually returns to the initial state, producing a measurable signal and relaxation time. The transverse relaxation time T_2 is a typical measurable signal and is usually applied to analyze the characteristics of pores and fractures in porous materials. The transverse relaxation time T_2 of fluids in pores and fractures in coal and rock is proportional to the pore radius r_c, with a larger pore corresponding to a longer relaxation time T_2 [55]. The characterization of porosity is based on a calibration curve for a standard sample. Through the Carr-Purcell-Meiboom-Gill (CPMG) sequence of the NMR system, the quantity of the NMR signal collected from the crushed outburst-prone coal after SHPB tests is compared with the quantity of the NMR signal on the calibration curve.

When the coal sample is in a uniform magnetic field, the transverse relaxation time T_2 is proportional to the pore radius, which can be expressed as [56]:

$$\frac{1}{T_2} = \rho_2 \frac{S}{V} = F_s \frac{\rho_2}{r_c} \tag{5}$$

where ρ_2 is the surface transverse relaxation rate, m/s; S is the surface area of coal rock pores, m^2; V is the volume of coal rock pores, m^3; F_s is the pore geometry morphologic factor, with $F_s = 2$ for column model and $F_s = 3$ for spherical pores; and r_c is the estimated pore size corresponding to a T2 value, m. In addition, the T_2 value reflects the fluid information within the pore structure in the coal sample. The T_2 value in different pore sizes is different. This allows the recovery of the porosity characteristics of the outburst-prone coal.

For NMR tests, the high-pressure gas coil with 70 mm in diameter was selected as the nuclear magnetic coil probe. The CPMG sequence was used to collect signals, with an echo time of TE = 0.205 ms, waiting time of TW = 5000 ms, echo number of NECH = 8000, and repeated sampling number of NS = 128. Coal samples were prepared into 60–80 mesh pulverized coal in the laboratory. In order to remove the influence of moisture on the NMR signal, the coal samples were dried in a vacuum oven at 80 °C for 4 h before the tests. The pulverized coal with a mass of 19.20 g was loaded into the chamber of the NMR gripper. After that, the coal chamber of the NMR gripper was vacuumized for 30 min. At room temperature, gas with a pressure of 1.0 MPa was injected into the coal sample to fully absorb the gas, and the nuclear magnetic signal was monitored dynamically. The coal sample was replaced, and the above steps were repeated until all the coal samples were completed.

3. Results and Discussion

To identify the contrasting dynamic failure characteristics separating outburst-prone from outburst-resistant coals and better understand the dynamic failure process, several uniaxial compressive SHPB tests were completed. A group of 14 coal specimens (Y1–Y14) from the Xintian (outburst-prone) coal mine were loaded to failure, with measured average strain rates varying from 17.18/s to 110.73/s; as a comparison, another group of seven coal specimens (X1–X7) from the Xinzhouyao (outburst-resistant) coal mine were also conducted, with the measured average strain rates varying from 22.76/s to 105.54/s.

3.1. Effect of Strain Rate on Dynamic Mechanical Properties

The dynamic stress-strain curves of Xinzhouyao and Xintian coal specimens under compressive SHPB tests are displayed in Figure 4. The compressive stress and strain of coal specimens with outburst-prone or resistant had significant strain-rate-dependent behavior. For instance, the peak compressive stress of Xinzhouyao specimen increased from 12.59 MPa to 47.79 MPa, while that of Xintian specimen increased from 5.23 MPa to 26.12 MPa.

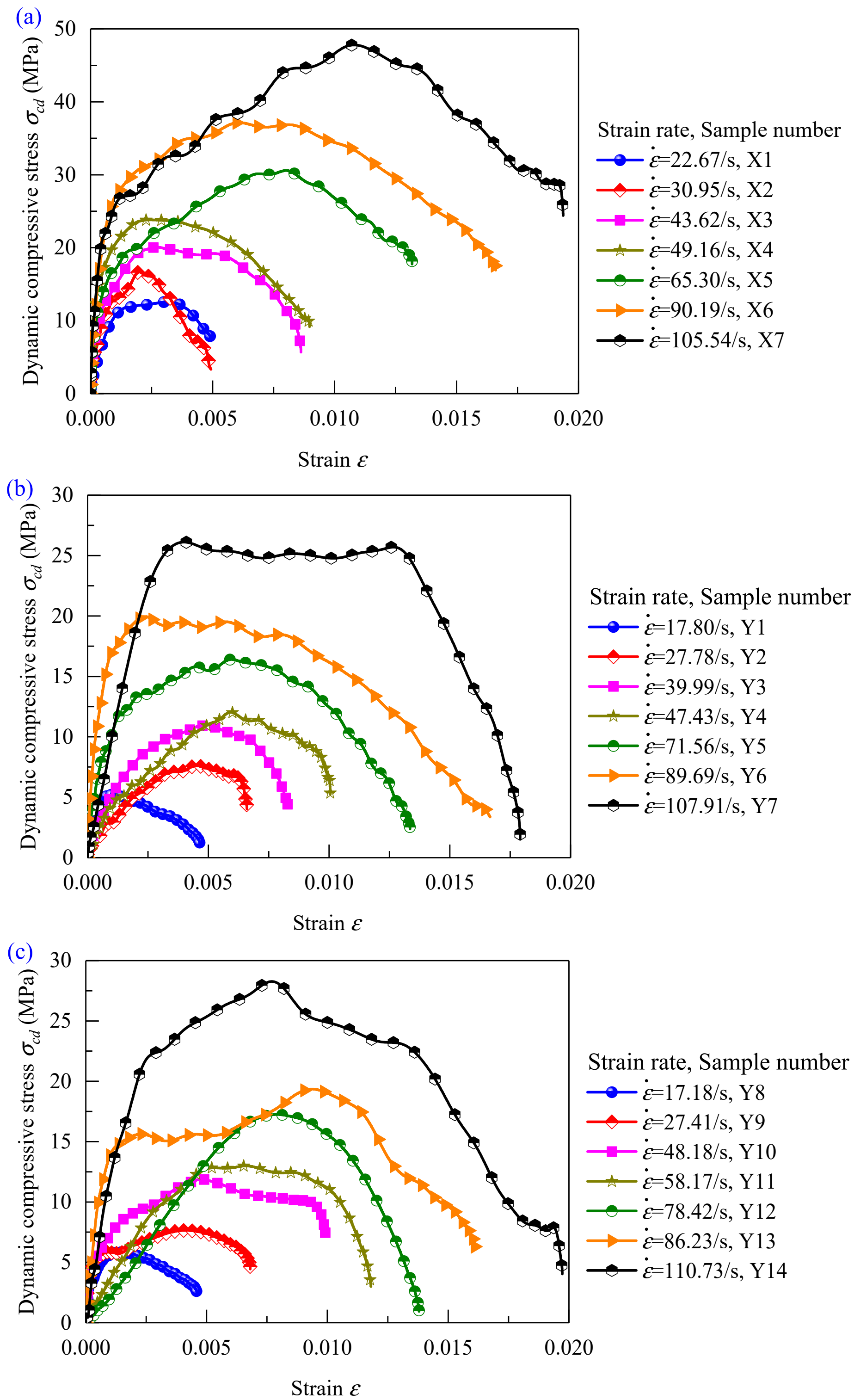

Figure 4. Dynamic stress-strain curves of (**a**) Xinzhouyao (outburst-resistant) coal specimens, (**b**) and (**c**) Xintian (outburst-prone) coal specimens in compressive SHPB test.

Compared with Xinzhouyao (resistant) coal, the Xintian (prone) coal had a smaller uniaxial compressive strength, implying that the outburst-prone coal was usually weaker in compression than the outburst-resistant coal.

Based on the features of the stress-strain curves presented in Figure 4, we provided a complete and typical curve to characterize the feature of the dynamic stress-strain relations of outburst-prone coal under different strain rates, as shown in Figure 5. As coal is one of the brittle rock materials, the typical dynamic stress-strain curve (failure process) is composed of five stages.

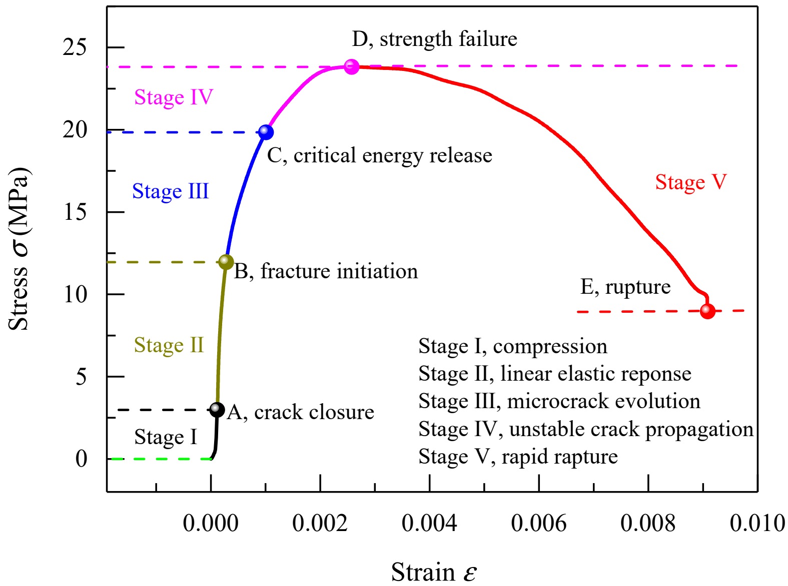

Figure 5. Characteristic composite stress-strain constitutive curve of coal specimen in SHPB test—assembled based on dominant processes acting at different stages of loading and unloading.

In stage I (compression), the stress-strain curve performs a concave feature. Two reasons are accounted for this feature: (1) the space between the pressure bar and specimen is gradually compacted, and (2) the micro-cracks inside coal specimens are closed (point A). The anti-deforming capability of coal specimen is increasing at the macro level. In stage II (linear elasticity), the stress-strain curve has a linear upward change feature. The stress wave is reflected repeatedly in the coal specimen to achieve stress homogeneity. The external load is insufficient to promote the crack propagation or produce new cracks in the specimen, that it can only make a steady-state deformation in the coal specimen with original cracks. The slope of this stage is used as the dynamic elastic modulus of the coal specimen. In stage III (micro-crack evolution), the stress increases slowly with the strain, and the curve is convex. As the impact loads increase continually, the micro-cracks in the specimen gradually propagate, and new fractures initiate (point B). In stage IV (unstable crack propagation), the stress acting on the coal specimen is about the peak value of the semi-sinusoidal elastic wave. Accompanied by the release of aggregated energy (point C), the fractures propagate rapidly, and new fractures are connected with the main fracture and eventually lead to the penetration of the specimen. At the end of this stage (point D), the stress on the specimen reaches the maximum value. Here, the peak stress appears with a corresponding peak strain. In stage V (rapid rapture), the carrying capacity of the specimen decreases rapidly. Because of the rapid deformation of the broken sample, the contact between the pressure bar and the sample is much complex, resulting in a large variation in curve features of different samples.

In Figure 4, the peak compressive stress increased with the strain rate. However, some other characteristic parameters were different for each curve. The micro-crack evolution and unstable crack propagation stage (stages III and IV) would prolong in both time and strain with the rising of strain rate. In other words, under high strain rate conditions, the cracks in coal specimens propagated and initiated more rapidly with advantages of spatial extension and temporal duration, which would cause more stored energy to dissipate during these two stages. After stage IV, curves of different strain rates entered the rapid unloading stage.

3.2. Effect of Strain Rate on Fragment Size Distribution

Figure 6 displays the fragmented shapes of outburst-prone and resistant coals after compressive SHPB tests. All specimens were loaded, through failure, at the applied strain rates. The specimen fragments showed different failure features and rupture degrees under different strain rates. When the impact loading was relatively low, the primary cracks within the specimen extended to rupture the specimen along the axial direction. The secondary cracks were not well developed at this stage. The coal fragments were mainly split into columns or lamellar structures, typically along a rectangular failure surface—induced by tensile failure. Before the absorbed energy increased sufficiently to promote the initiation of new cracks, the preexisting micro-cracks extended with less energy consumption and propagated and penetrated to pre-rupture the specimen. In this instance, the specimens were comminuted, and the crushed coals were in large fragments. With an increase in the impact loading (strain rate), specimens absorbed more energy within a short time and released this energy, leading to the initiation of more secondary cracks in the dynamic failure process. Cone-shaped fragments of the triangular cross-section were mainly caused by shear failure. The generation of small fragments and the evolution of sheared surfaces increased with an increase in strain rate.

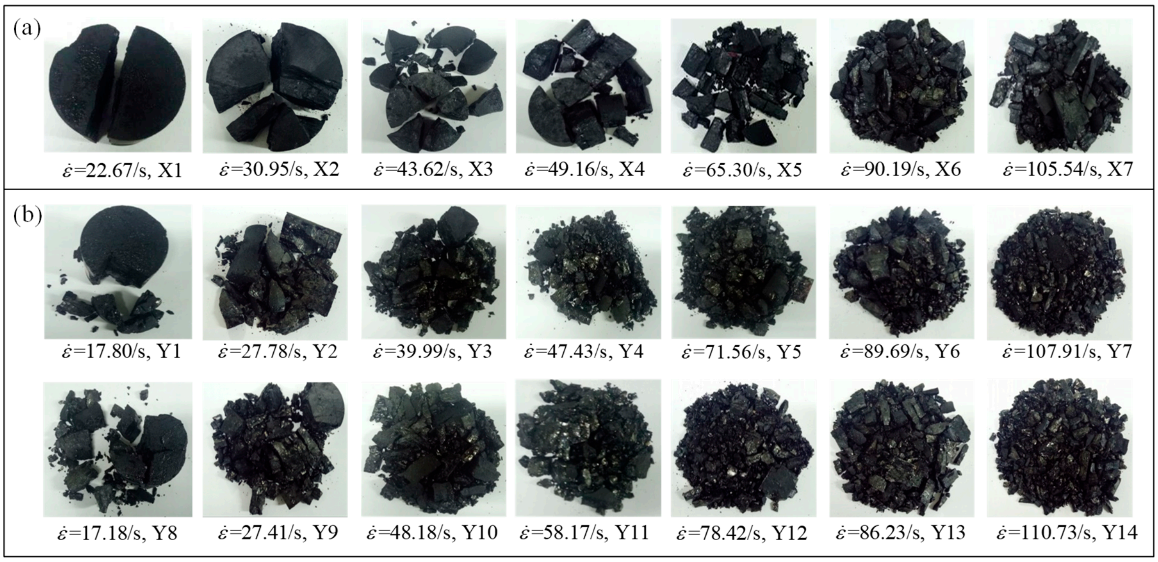

Figure 6. Fragment distribution of crushed coal in uniaxial compressive SHPB tests at different strain rates: (**a**) Xinzhouyao specimens (resistant), (**b**) Xintian specimens (prone).

To investigate the effect of strain rate on the comminution in outburst-prone and outburst-resistant coals, the fragments of crushed particles were analyzed. The crushed particles of each specimen were categorized into seven grades at 0~0.5 mm, 0.5~1 mm, 1~2 mm, 2~5 mm, 5~10 mm, 10~20 mm, 20~50 mm, as labeled n = 1, 2, 3, 4, 5, 6, and 7, respectively. The crushed coal samples were categorized by classifying sieves with different diameters (0.5 mm, 1 mm, 2 mm, 5 mm, 10 mm, and 20 mm). Specifically, first of all, the sieve with the largest diameter of 20 mm was used. The coal sample in the sieve would be weighted after being vibrated every 20 times. If the difference between the two weighings was less than 0.1 g, the screening requirements of this diameter of the sieve was reached. Then, the crushed coal sample under the current sieve was put into a smaller size sieve. According to the above method, the grain fractions of crushed coal were separated until the coal sample was screened by the minimum size of 0.5 mm of classifying sieve.

We defined the equivalent particle size of the crushed coal specimen as:

$$r = \sum_{n=1}^{7} W_{sn} d_{vn} \tag{6}$$

where r is the equivalent particle size, mm; d_{vn} represents the average particle size of each grade, mm; and W_{sn} is the particle mass ratio, which is defined as the mass percent of each particle grade accounted for the whole specimen. The equivalent particle size described the degree of specimen failure, with a smaller value corresponding to smaller average particle size and a higher level of comminution.

In Figure 7, the fragments at low strain rates are mainly distributed in size range 20~50 mm. The increasing strain rate broadened the size distribution of coal fragments. The particle mass ratio in size range of the small particles increased, while that in the large particle size range decreased. For example, the particle mass ratio over the minimum size range (0~0.5 mm) of the Xintian specimen Y8 ($\dot{\varepsilon}$ = 17.18/s) was ~0.00%, and this value for specimens Y9 ($\dot{\varepsilon}$ = 27.41/s) and Y14 ($\dot{\varepsilon}$ = 110.73/s) were ~0.24% and ~6.77%, respectively. Conversely, the particle mass ratio in the maximum size range (20~50 mm) decreased from 62.46% to 14.95% when the strain rate increased from 17.18/s (Y8) to 48.18/s (Y10). According to Equation (5), the equivalent particle sizes r at different strain rates were calculated, as shown in Figure 7. The equivalent particle size of coal fragments decreased with the strain rate. For Xintian coal (prone), when the strain rate rose from 17.18/s (Y8) to 110.73/s (Y14), the equivalent particle size decreased from 25.85 mm to 4.51 mm, representing a reduction of 5.73 times. Compared with Xintian coal (prone), the equivalent particle size of the Xinzhouyao coal (resistant) was larger.

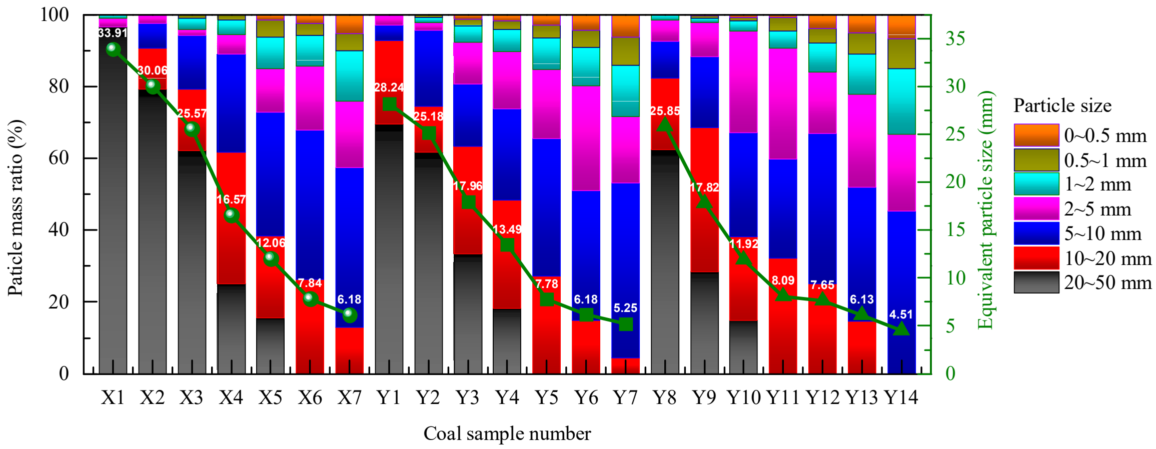

Figure 7. Particle mass ratio and equivalent particle size of crushed coal under uniaxial compressive SHPB tests—specimens X1–X7 are for Xinzhouyao coal (resistant), and specimens Y1–Y14 are for Xintian coal (prone).

From the above, we noted that larger impact loading (strain rate) would cause greater damage to the coal specimens, as is manifest in the greater mass proportion of pulverized coal. Under similar impact loading, the cracks within outburst-prone coals developed and aggregated more readily, resulting in smaller equivalent particle size for the outburst-prone coals relative to outburst-resistant coals.

3.3. Effect of Strain Rate on Microstructural Characteristics

The macroscopic mechanical properties of the outburst-prone (resistant) coals are closely related to their microstructural characteristics. Hence, we used SEM and NMR imaging to study the microstructural characteristics of the dynamically failed coal.

SEM images of the crushed coal following the compressive SHPB tests were shown for four outburst-prone specimens (Y1, Y3, Y5, Y7) and four outburst-resistant specimens (X1, X3, X5, X7). These were shown at a magnification of 1500 and 500 (Figure 8). The microstructure changed dramatically with the strain rate. When the strain rate was low, only a few isolated pores could be observed, and the distribution of pores and fractures was dispersed. This indicated that the connectivity among pores and fractures within the specimens was poor when subjected to only low dynamic loading. As the strain rate increased, the observed pores and fractures increased, as well as developing some defects on the coal particle surface. The primary fractures expanded to become secondary fractures and to cause several fractures penetrating through pores. For example, in coal specimen Y5 ($\dot{\varepsilon}$ = 71.56/s), the primary fractures expanded and propagated through the laterally isolated pores. As a result, the connectivity between pores and fractures was enhanced. Under dynamic loading at high strain rates, such as in gas outbursting, the evolution of microstructures in the coal mass was illustrated by the expansion of pores, the propagation of primary fractures, and the generation of secondary fractures.

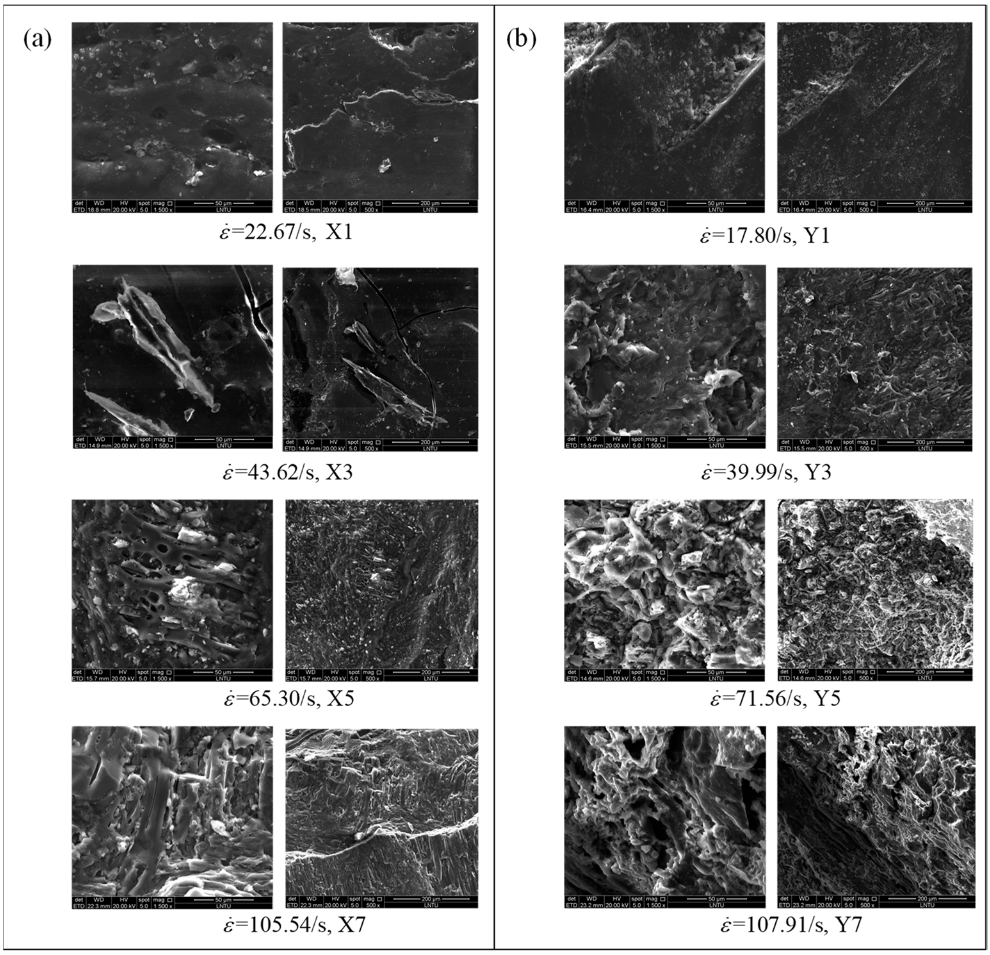

Figure 8. Scanning electron microscope (SEM) images of coal specimens failed at different strain rates: (**a**) Xinzhouyao coal (resistant), and (**b**) Xintian coal (prone).

According to the International Union of Pure and Applied Chemistry (UIPAC) classification and characteristics of gas flow in pores, the microstructure within the coal specimen can be divided into micropores (<2 nm), mesopores (2–50 nm), macropores (50–10^3 nm), super macropores (10^3–10^4 nm), and fractures (>10^4 nm), based on pore size [57,58]. Figure 9 shows the pore size distribution of Xintian coal (outburst-prone) after comminution through compressive SHPB tests under varying strain rates. All the curves in Figure 9 were characterized by three peaks, from left to right representing meso-macropores (mesopores and macropores), super macropores, and fractures, respectively. The peaks for the meso-macropores and fractures were higher than those for the super macropores, implying that the meso-macropores and fractures within the outburst-prone coal were more fully developed, following dynamic failure. The peak in the meso-macropores decreased with the increase of strain rate, while the peak for the fractures increased. When coals were subjected to dynamic loading under a high strain rate, the coal matrix failed in either compression or tension. As a result of this, some new meso-macropores formed in the coal matrix, while preexisting meso-macropores extended into super-macropores and fractures. The combined result of these two processes was that the proportion of meso-macropores decreased, and the proportion of fractures increased. Although the proportion of meso-macropores decreased at a high strain rate, the volume of meso-macropores still increased when compared with low strain rates. Therefore, a high strain rate led to a greater development of the fractures within the crushed coal and a greater enhancement in coal permeability.

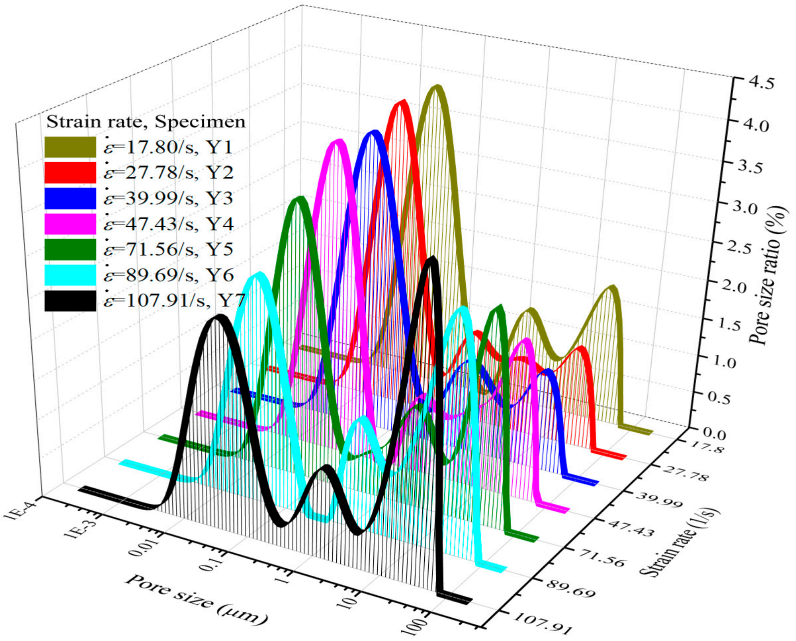

Figure 9. The pore size distribution of Xintian coal specimens (prone) at different strain rates.

Figure 10 shows the pore throat distribution of Xintian coal specimens after SHPB tests at different strain rates. The pore throat in the diameter range of 0.25–0.63 μm occupied only a small proportion of the total. The ratio of pore throats with a diameter <0.1 μm or >10 μm was relatively large, indicating that the pore throats in this range were well developed and that both the pores and fractures were well connected.

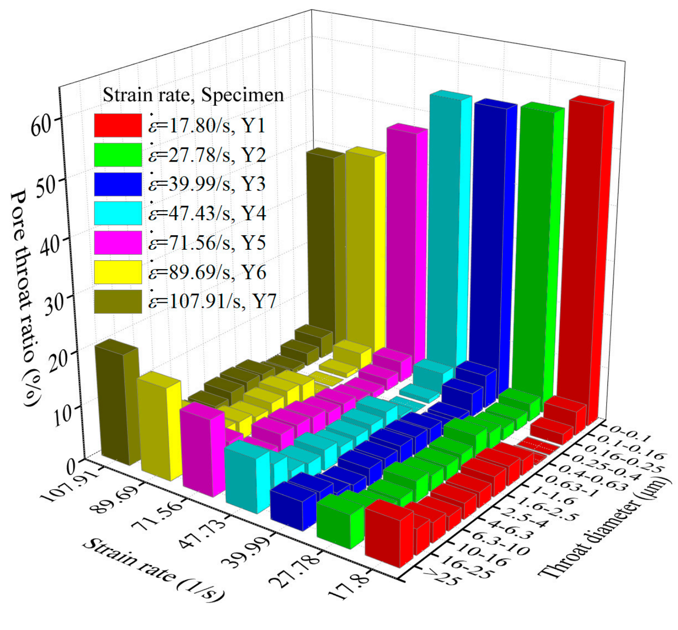

Figure 10. Pore throat distributions at different strain rates within crushed specimens of Xintian coal (prone).

Many scholars [59,60] have verified that the most types of pores are a bottle or cylindrical pores, which can seal more gas within coal seam, and thus form high gas pressure to promote a coal and gas outburst disaster. Therefore, we designated the pore throat to describe the connection between pores. As displayed in Table 2, the distribution of pore throat diameters was dominated by micro-throats, accounting for 38.85%–58.14% of the total of throats. The ratio of pore throats with a diameter <0.1 μm decreased with increased strain rate, and the ratio of pore throats with a diameter >10 μm initially slightly decreased and then rapidly increased with strain rate. For example, the ratio of pore throats >10 μm in diameter reached 36.01% when the strain rate increased to 107.91/s. These pore throats connect pores and fractures and increase the coal permeability [61], to provide a favorable condition for rapid gas emission.

Table 2. The proportion of micro- and macro- throats within crushed specimens of Xintian coal.

Specimen Number	Average Strain Rate (1/s)	<0.1 μm Throat Ratio (%)	>10 μm Throat Ratio (%)
Y1	17.80	58.14	16.35
Y2	27.78	55.45	13.44
Y3	39.99	54.54	12.94
Y4	47.43	54.53	20.58
Y5	71.56	46.84	25.18
Y6	89.69	40.75	33.11
Y7	107.91	38.85	36.01

It was found that the compressive strength of outburst-prone coal was lower than that of outburst-resistant coal under the same impact load or strain rate. When the coal mass was subjected to the impact load, the stress wave transported within the coal mass to form stress concentration near the pores and fractures, driving the original pores, and fractures expanded, resulting in many secondary fractures. The impact load promoted the development of pores and fractures and enhanced the connectivity of pores and fractures. Due to the development of secondary fractures, the velocity of the desorbed gas from the coal matrix to cracks increased, leading to a large number of free gas transports into the fractures to increase the fracture pressure and further accelerate the destruction of coal. Therefore, the outburst-prone coal was characterized by the low mechanical properties and sudden increase of permeability when dynamically destroyed, which can easily initiate gas outbursts.

4. Conclusions

In this paper, dynamic uniaxial compressive tests were conducted on both outburst-prone and resistant coals by the SHPB system. The dynamic failure characteristics, including the dynamic strength, failure process, crushed coal fragment, and microcosmic pore distribution, were comparatively analyzed. Some conclusions can be drawn:

(1) The dynamic stress-strain response of specimens primarily comprised stages of compression, linear elastic deformation then, micro-crack evolution, followed by unstable crack propagation, culminating in rapid unloading. The compressive strength inclined linearly with the applied strain rate.
(2) When the impact loading rate was relatively low, only the micro-cracks consuming reduced energy adsorption participated in rupturing the coal specimen, and fragments failed in tension as apparent in the development of a typical tensile failure surface. With the impact's stress increasing, the fragments failed predominantly in shear. The equivalent particle size of the coal fragments decreased with the applied strain rate. The equivalent particle size of outburst-prone coal was smaller than that of outburst-resistant coal.
(3) Observed by the SEM and NMR, the microstructure changed dramatically with the strain rates. When the impact load was low, the pores and fractures were mainly isolated, and the

connectivity between them was poor. As the impact load increased, the primary fractures expanded and propagated through the isolated pores, causing numerous pores to break to form secondary fractures.

(4) With the increase of strain rate, the proportion of fractures in coal tended to increase, the ratio of pore throat with diameter <0.1 μm decreased, and the ratio of pore throat with diameter >10 μm firstly decreased slightly and then increased rapidly.

Author Contributions: All authors contributed equally to this work. Z.Y., S.L., T.L., C.F., G.W., M.L., and H.Z. are the main authors of this work. Z.Y., C.F., and M.L. wrote the paper. S.L., T.L., G.W., and H.Z. supported the research in terms of both scientific and technical expertise. All authors have been involved in the manuscript preparation.

Funding: This research was financially supported by the National Natural Science Foundation of China (Grant Nos. 51674132, 51874159, and 51674135), the Research Fund of State Key Laboratory of Coal Resources and Safe Mining, CUMT (Grant No. SKLCRSM18KF000), and the Project supported by the Postdoctoral Science Foundation of China (Grant No. 2018M641675).

Acknowledgments: The author(s) would like to thank all editors and anonymous reviewers for their comments and suggestions.

Conflicts of Interest: The authors declare no competing financial interest.

References

1. Beamish, B.B.; Crosdale, P.J. Instantaneous outbursts in underground coal mines: An overview and association with coal type. *Int. J. Coal Geol.* **1998**, *35*, 27–55. [CrossRef]
2. Xu, T.; Tang, C.A.; Yang, T.H.; Zhu, W.C.; Liu, J. Numerical investigation of coal and gas outbursts in underground collieries. *Int. J. Rock Mech. Min. Sci.* **2006**, *43*, 905–919. [CrossRef]
3. Liu, T.; Lin, B.; Yang, W.; Zou, Q.; Jia, K.; Yan, F. Cracking process and stress field evolution in specimen containing combined flaw under uniaxial compression. *Rock Mech. Rock Eng.* **2016**, *49*, 3095–3113. [CrossRef]
4. Lama, R.D.; Bodziony, J. Management of outburst in underground coal mines. *Int. J. Coal Geol.* **1998**, *35*, 83–115. [CrossRef]
5. Wang, G.; Gong, S.; Dou, L.; Cai, W.; Jin, F.; Fan, C. Behaviour and bursting failure of roadways based on a pendulum impact test facility. *Tunn. Undergr. Space Technol.* **2019**, *92*, 103042. [CrossRef]
6. Wang, G.; Gong, S.; Dou, L.; Cai, W.; Yuan, X.; Fan, C. Rockburst mechanism and control in coal seam with both syncline and hard strata. *Saf. Sci.* **2019**, *115*, 320–328. [CrossRef]
7. Wang, G.; Jin, F.; Gong, S.; Dou, L.; Fan, C.; Cai, W.; Yuan, X. Generating behaviors of strong tremors and experimental study of rockburst-triggering criterion. *Shock Vib.* **2019**, *2019*, 6319612. [CrossRef]
8. Fan, C.; Li, S.; Luo, M.; Yang, Z.; Lan, T. Numerical simulation of hydraulic fracturing in coal seam for enhancing underground gas drainage. *Energ. Explor. Exploit.* **2019**, *37*, 166–193. [CrossRef]
9. Fan, C.; Li, S.; Luo, M.; Du, W.; Yang, Z. Coal and gas outburst dynamic system. *Int. J. Min. Sci. Technol.* **2017**, *27*, 49–55. [CrossRef]
10. Zhao, W.; Cheng, Y.; Guo, P.; Jin, K.; Tu, Q.; Wang, H. An analysis of the gas-solid plug flow formation: New insights into the coal failure process during coal and gas outbursts. *Powder Technol.* **2017**, *305*, 39–47. [CrossRef]
11. Yin, G.; Jiang, C.; Wang, J.G.; Xu, J.; Zhang, D.; Huang, G. A new experimental apparatus for coal and gas outburst simulation. *Rock Mech. Rock Eng.* **2016**, *49*, 2005–2013. [CrossRef]
12. Zhao, W.; Cheng, Y.; Jiang, H.; Jin, K.; Wang, H.; Wang, L. Role of the rapid gas desorption of coal powders in the development stage of outbursts. *J. Nat. Gas Sci. Eng.* **2016**, *28*, 491–501. [CrossRef]
13. Xue, Y.; Gao, F.; Liu, X. Effect of damage evolution of coal on permeability variation and analysis of gas outburst hazard with coal mining. *Nat. Hazards* **2015**, *79*, 999–1013. [CrossRef]
14. Fan, C.; Elsworth, D.; Li, S.; Zhou, L.; Yang, Z.; Song, Y. Thermo-hydro-mechanical-chemical couplings controlling CH_4 production and CO_2 sequestration in enhanced coalbed methane recovery. *Energy* **2019**, *173*, 1054–1077. [CrossRef]
15. Liu, H.; Lin, B.; Mou, J.; Yang, W. Mechanical evolution mechanism of coal and gas outburst. *Rock Mech. Rock Eng.* **2019**, *52*, 1591–1597. [CrossRef]

16. An, F.; Yuan, Y.; Chen, X.; Li, Z.; Li, L. Expansion energy of coal gas for the initiation of coal and gas outbursts. *Fuel* **2019**, *235*, 551–557. [CrossRef]
17. Han, J.; Zhang, H. The controlling of tectonic evolution to coal and gas outburst. *J. China Coal Soc.* **2010**, *35*, 1125–1130.
18. Wang, G.; Qin, X.; Shen, J.; Zhang, Z.; Han, D.; Jiang, C. Quantitative analysis of microscopic structure and gas seepage characteristics of low-rank coal based on CT three-dimensional reconstruction of CT images and fractal theory. *Fuel* **2019**, *256*, 115900. [CrossRef]
19. Wang, G.; Jiang, C.; Shen, J.; Han, D.; Qin, X. Deformation and water transport behaviors study of heterogenous coal using CT-based 3D simulation. *Int. J. Coal Geol.* **2019**, *211*, 103204. [CrossRef]
20. Li, H.; Shi, S.; Lu, J.; Ye, Q.; Lu, Y.; Zhu, X. Pore structure and multifractal analysis of coal subjected to microwave heating. *Powder Technol.* **2019**, *346*, 97–108. [CrossRef]
21. Li, H.; Shi, S.; Lin, B.; Lu, J.; Lu, Y.; Ye, Q.; Wang, Z.; Hong, Y.; Zhu, X. A fully coupled electromagnetic, heat transfer and multiphase porous media model for microwave heating of coal. *Fuel Process. Technol.* **2019**, *189*, 49–61. [CrossRef]
22. Huang, Q.; Liu, S.; Wang, G.; Wu, B.; Yang, Y.; Liu, Y. Gas sorption and diffusion damages by guar-based fracturing fluid for CBM reservoirs. *Fuel* **2019**, *251*, 30–44. [CrossRef]
23. Song, Y.; Jiang, B.; Lan, F. Competitive adsorption of CO_2/N2/CH_4 onto coal vitrinite macromolecular: Effects of electrostatic interactions and oxygen functionalities. *Fuel* **2019**, *235*, 23–38.
24. Fan, C.; Elsworth, D.; Li, S.; Chen, Z.; Luo, M.; Song, Y.; Zhang, H. Modelling and optimization of enhanced coalbed methane recovery using CO_2/N2 mixtures. *Fuel* **2019**, *253*, 1114–1129. [CrossRef]
25. Norbert, S.; Pajdak, A.; Kozieł, K.; Braga, L.T.P. Methane emission during gas and rock outburst on the basis of the unipore model. *Energies* **2019**, *12*, 1999. [CrossRef]
26. Skoczylas, N. Coal Seam Methane Pressure as a Parameter Determining the Level of the Outburst Risk–Laboratory and in Situ Research. *Arch. Min. Sci.* **2012**, *57*, 861–869.
27. Song, H.; Jiang, Y.; Elsworth, D.; Zhao, Y.; Wang, J.; Liu, B. Scale effects and strength anisotropy in coal. *Int. J. Coal Geol.* **2018**, *195*, 37–46. [CrossRef]
28. Singh, J.G. A mechanism of outbursts of coal and gas. *Min. Sci. Technol.* **1984**, *1*, 269–273. [CrossRef]
29. Li, H.; Shi, S.; Lin, B.; Lu, J.; Ye, Q.; Lu, Y.; Zhu, X. Effects of microwave-assisted pyrolysis on the microstructure of bituminous coals. *Energy* **2019**, *187*, 115986. [CrossRef]
30. Barker-read, G.R.; Radchenko, S.A. The relationship between the pore structure of coal and gas-dynamic behaviour of coal seams. *Min. Sci. Technol.* **1989**, *8*, 109–131. [CrossRef]
31. Xia, K.; Huang, S.; Jha, A.K. Dynamic tensile test of coal, shale and sandstone using split Hopkinson pressure bar: A tool for blast and impact assessment. *Int. J. Geotech. Earthq. Eng.* **2010**, *1*, 24–37. [CrossRef]
32. Feng, J.; Wang, E.; Chen, X.; Ding, H. Energy dissipation rate: An indicator of coal deformation and failure under static and dynamic compressive loads. *Int. J. Min. Sci. Technol.* **2018**, *28*, 397–406. [CrossRef]
33. Fakhimi, A.; Azhdari, P.; Kimberley, J. Physical and numerical evaluation of rock strength in Split Hopkinson Pressure Bar testing. *Comput. Geotech.* **2018**, *102*, 1–11. [CrossRef]
34. Ju, Y.; Sudak, L.; Xie, H. Study on stress wave propagation in fractured rocks with fractal joint surfaces. *Int. J. Solids Struct.* **2007**, *44*, 4256–4271. [CrossRef]
35. Feng, J.; Wang, E.; Chen, L.; Li, X.; Xu, Z.; Li, G. Experimental study of the stress effect on attenuation of normally incident P-wave through coal. *J. Appl. Geophys.* **2016**, *132*, 25–32. [CrossRef]
36. Zhou, Z.; Cai, X.; Ma, D.; Du, X.; Chen, L.; Wang, H.; Zang, H. Water saturation effects on dynamic fracture behavior of sandstone. *Int. J. Rock Mech. Min.* **2019**, *114*, 46–61. [CrossRef]
37. Zhou, Z.; Cai, X.; Ma, D.; Chen, L.; Wang, S.; Tan, L. Dynamic tensile properties of sandstone subjected to wetting and drying cycles. *Constr. Build. Mater.* **2018**, *182*, 215–232. [CrossRef]
38. Li, M.; Lin, G.; Zhou, W.; Mao, X.; Zhang, L.; Mao, R. Experimental study on dynamic tensile failure of sandstone specimens with different water contents. *Shock Vib.* **2019**, *2019*, 7012752. [CrossRef]
39. Ma, D.; Rezania, M.; Yu, H.; Bai, H. Variations of hydraulic properties of granular sandstones during water inrush: Effect of small particle migration. *Eng. Geol.* **2017**, *217*, 61–70. [CrossRef]
40. Liu, M.; He, X. Electromagnetic response of outburst-prone coal. *Int. J. Coal Geol.* **2001**, *45*, 155–162.
41. Jiang, C.; Xu, L.; Li, X.; Tang, J.; Chen, Y.; Tian, S.; Liu, H. Identification model and indicator of outburst-prone coal seams. *Rock Mech. Rock Eng.* **2015**, *48*, 409–415. [CrossRef]

42. Qi, L.; Tang, X.; Wang, Z.; Peng, X. Pore characterization of different types of coal from coal and gas outburst disaster sites using low temperature nitrogen adsorption approach. *Int. J. Min. Sci. Technol.* **2017**, *27*, 371–377. [CrossRef]
43. Zhao, Y.; Gong, S.; Hao, X.; Peng, Y.; Jiang, Y. Effects of loading rate and bedding on the dynamic fracture toughness of coal: Laboratory experiments. *Eng. Fract. Mech.* **2017**, *178*, 375–391. [CrossRef]
44. Xia, K.; Yao, W. Dynamic rock tests using split Hopkinson (Kolsky) bar system—A review. *J. Rock. Mech. Geotech. Eng.* **2015**, *7*, 27–59. [CrossRef]
45. Li, M.; Mao, X.; Lu, A.; Tao, J.; Zhang, G.; Zhang, L.; Li, C. Effect of specimen size on energy dissipation characteristics of red sandstone under high strain rate. *Int. J. Min. Sci. Technol.* **2014**, *24*, 151–156. [CrossRef]
46. Wang, W.; Wang, H.; Li, D.; Li, H.; Liu, Z. Strength and failure characteristics of natural and water-saturated coal specimens under static and dynamic loads. *Shock Vib.* **2018**, *2018*, 3526121. [CrossRef]
47. Luo, X.; Xu, J.Y.; Bai, E.L.; Li, W. Research on the dynamic compressive test of highly fluidized geopolymer concrete. *Constr. Build. Mater.* **2013**, *48*, 166–172. [CrossRef]
48. Frew, D.J.; Forrestal, M.J.; Chen, W. Pulse shaping techniques for testing brittle materials with a split Hopkinson pressure bar. *Exp. Mech.* **2002**, *42*, 93–106. [CrossRef]
49. Li, M.; Mao, X.; Cao, L.; Pu, H.; Mao, R.; Lu, A. Effects of thermal treatment on the dynamic mechanical properties of coal measures sandstone. *Rock Mech. Rock Eng.* **2016**, *49*, 3525–3539. [CrossRef]
50. Huo, B.; Jing, X.; Fan, C.; Han, Y. Numerical investigation of flue gas injection enhanced underground coal seam gas drainage. *Energy Sci. Eng.* **2019**. [CrossRef]
51. Li, C.; Wei, S.; Wang, X.; Liu, J.; Lei, D. Experiment of dynamic property and transient magnetic effects of coal during deformation and fracture. *J. Coal Sci. Eng.* **2012**, *18*, 258–261. [CrossRef]
52. Zhao, Y.; Gong, S.; Zhang, C.; Zhang, Z.; Jiang, Y. Fractal characteristics of crack propagation in coal under impact loading. *Fractals* **2018**, *26*, 1840014. [CrossRef]
53. Li, C.; Wang, Q.; Lyu, P. Study on electromagnetic radiation and mechanical characteristics of coal during an SHPB test. *J. Geophys. Eng.* **2016**, *13*, 391–398.
54. ISRM. The complete ISRM suggested methods for rock characterization, testing and monitoring: 1974–2006. *Int. Soc. Rock Mech. Comm. Test Methods* **2007**, *15*, 47–48.
55. Yao, Y.; Liu, D.; Cai, Y.; Li, J. Advanced characterization of pores and fractures in coals by nuclear magnetic resonance and X-ray computed tomography. *Sci. China Earth Sci.* **2010**, *53*, 854–862. [CrossRef]
56. Yao, Y.; Liu, D.; Che, Y.; Tang, D.; Tang, S.; Huang, W. Petrophysical characterization of coals by low-field nuclear magnetic resonance (NMR). *Fuel* **2010**, *89*, 1371–1380. [CrossRef]
57. Cai, Y.; Liu, D.; Pan, Z.; Yao, Y.; Li, J.; Qiu, Y. Pore structure and its impact on CH_4 adsorption capacity and flow capability of bituminous and subbituminous coals from Northeast China. *Fuel* **2013**, *103*, 258–268. [CrossRef]
58. Sing, K.S.W. Reporting physisorption data for gas/solid systems with special reference to the determination of surface area and porosity (Recommendations 1984). *Pure Appl. Chem.* **1985**, *57*, 603–619. [CrossRef]
59. Yu, S.; Bo, J.; Pei, S.; Jiahao, W. Matrix compression and multifractal characterization for tectonically deformed coals by Hg porosimetry. *Fuel* **2018**, *211*, 661–675. [CrossRef]
60. Yu, S.; Bo, J.; Jie-gang, L. Nanopore structural characteristics and their impact on methane adsorption and diffusion in low to medium tectonically deformed coals: Case study in the Huaibei coal field. *Energy Fuel* **2017**, *31*, 6711–6723. [CrossRef]
61. Wang, L.; Chen, Z.; Wang, C.; Elsworth, D.; Liu, W. Reassessment of coal permeability evolution using steady-state flow methods: The role of flow regime transition. *Int. J. Coal Geol.* **2019**, *211*, 103210. [CrossRef]